

Newtonian propagation methods applied to the photodissociation dynamics of I_3^-

Guy Ashkenazi, Ronnie Kosloff, Sanford Ruhman, and Hillel Tal-Ezer

Department of Physical Chemistry and the Fritz Haber Research Center, The Hebrew University, Jerusalem 91904, Israel

(Received 14 July 1995; accepted 11 September 1995)

A uniformly convergent propagation scheme designed for non-Hermitian Hamiltonian operators is presented. The method is based on a Newtonian interpolation polynomial which is created by a recursive application of the Hamiltonian operator on an initial wave function. The interpolation points used to construct the Newtonian polynomial are located in the complex eigenvalue space of the Hamiltonian. A new algorithm is developed to construct the interpolation points. Both time dependent and time independent quantities can be obtained using the same polynomial expansion. The method is particularly useful when negative imaginary potentials are used. The photodissociation dynamics of I_3^- is studied as an example of the utility of the scheme to gain insight on a dynamical encounter. The bond cleavage is followed in time simultaneously with the calculation of the Raman spectra. The study addresses the role of vibrational excitation of the reactant I_3^- on the nascent I_2^- spectral modulations and Raman spectra. © 1995 American Institute of Physics.

I. INTRODUCTION

When a UV light pulse is applied to triiodide in solution, it either absorbs the light leading to fragmentation to $I_2^- + I$, or emits light in a Raman or fluorescence process. Since both the fragmentation and the Raman processes are governed by the same ground and excited potential energy surfaces, crossing the information gained from the two independent measurements leads to enhanced insight on the photodissociation event. The elucidation of the dynamical encounter requires a quantum framework. The purpose of this paper is to present a unified quantum computational scheme which simultaneously addresses the dynamics of photodissociation and the absorption and Raman cross sections.

The main idea behind the quantum simulation is that the ground state wave function is a common starting point for calculating all relevant observables. From this starting point the Hamiltonian generates all dynamical behavior. This means that by recursively applying the Hamiltonian to the initial wave function all the dynamical behavior can in principle be reconstructed. For this procedure to work, a uniformly convergent method has to be applied to sum the power series into the different final results. The Chebychev polynomial expansion has uniform convergence properties and therefore has been utilized in both time dependent and time independent calculations starting from the same initial wave function. The need to limit the size of the spatial description and to impose outgoing boundary conditions has led to the use of negative imaginary potentials. This in turn creates a non-Hermitian Hamiltonian. The purpose of this paper is to develop a simple uniformly convergent global propagation technique applicable to non-Hermitian operators. With this method time dependent and time independent properties can be calculated simultaneously using the same expansion.

The photo-induced processes of the I_3^- system in different solvents has been the subject of extensive experimental

and theoretical studies.¹⁻⁵ Of importance to this study are the coherent vibrations of the I_2^- product synchronized with the photo-excitation pulse.^{1,2,6} In conjunction with this process the leftover I_3^- reactant is also coherently excited due to the dynamical "hole" left on the ground surface.^{3,5} This vibration can be correlated to the Raman spectra of I_3^- .

To date the theoretical analysis of the triiodide experiments has proceeded along two paths. Both classical molecular dynamics⁴ and quantum simulations were initiated,² employing the same model for intramolecular potentials in both studies. The rationale behind conducting both efforts was the following. The quantum mechanical simulations allow one to envision the photodissociative dynamics of an isolated triiodide ion determined by the model potentials, including full quantum detail of the matter light interactions. This serves not only for critically appreciating the intramolecular consequences of impulsive optical excitation, but also serves as a chemical dynamical standard against which the results of molecular dynamics simulations may be contrasted in order to understand the effects of the solvent bath upon the reaction dynamics in solution.

In previous publications² quantum simulations were reported which provided the functional form and parameters of the potential surfaces, and presented initial simulations for temporal evolution of the zeroth vibronic ground state level upon instantaneous promotion to the excited reactive surface. The simulations presented here are aimed at improving three crucial points in modeling the reaction dynamics: to include the effects of the finite duration of the excitation and probing pulses, and that of starting the reaction with vibrationally excited reactants, into the previously described scheme. The latter is clearly of great importance in view of the fact that the quanta of all three vibrational modes are substantially lower than the thermal excitation energy kT at room temperature. After including these improvements an effort has been made to actually calculate the transient transmission

spectra for delayed probe pulses, which is the experimental observable collected in the laboratory.

II. PROPAGATION SCHEMES

Iterative propagation schemes have become the methods of choice in quantum dynamical modeling and simulations. The reason is their superior efficiency when the size of the problem increases. These schemes are based on the ability to perform numerically the elementary mapping step of a wave function induced by the Hamiltonian:

$$\phi = \hat{H}\psi. \quad (2.1)$$

The propagators are defined by their recursive application of the elementary mapping step.⁷ This amounts to approximating a function of the Hamiltonian as a polynomial.

Different methods have been developed to perform the elementary mapping. In the present study the Fourier method^{8,9} is employed to calculate the mapping of the wave function ψ induced by the Hamiltonian.

Our original propagation scheme¹⁰ was developed to solve the time dependent Schrödinger equation. The evolution operator $\hat{U}(t) = e^{-i\hat{H}t/\hbar}$ was approximated as a polynomial. A spectral expansion based on the Chebychev orthogonal polynomial was used leading to

$$\begin{aligned} \psi(t) &= e^{-i/\hbar \hat{H}t} \psi(0) \\ &\approx e^{-i/\hbar (\Delta E/2 + E_{\min})t} \sum_{n=0}^{N_{ch}-1} a_n \left(\frac{\Delta E t}{2\hbar} \right) T_n(\hat{H}_{\text{norm}}) \psi(0), \end{aligned} \quad (2.2)$$

where the expansion coefficients become $a_n(\alpha) = i^n (2 - \delta_{n0}) J_n(\alpha)$ and $T_n(x)$ are the Chebychev polynomials: $T_n(\cos \theta) = \cos(n\theta)$.⁷ For stability in Eq. (2.2) the Hamiltonian is normalized: $\hat{H}_{\text{norm}} = 2(\hat{H} - \bar{H})/\Delta E$ where $\bar{H} = (E_{\max} + E_{\min})/2$ is the center of the eigenvalue spectrum and $\Delta E = (E_{\max} - E_{\min})$ is the eigenvalue range of \hat{H} . The normalized Hamiltonian has its eigenvalues distributed on the real axis between -1 to 1 .

Examining Eq. (2.2) it can be noticed that the time variable only appears in the expansion coefficients a_n . The computationally intensive part, which is the evaluation of the mapping induced by the Chebychev polynomial $\phi_n = T_n(\hat{H}_{\text{norm}}) \psi(0)$, is time independent. This observation has led to the development of propagation schemes for other functions of the Hamiltonian. Examples include the Green's function, allowing the calculation of Raman spectra,¹¹ or reactive scattering cross sections,^{12,13} the delta function, allowing the calculation of absorption spectra¹⁴ and density of states,^{15,16} and propagation in imaginary time¹⁷ and filter diagonalization^{18–20} allowing the calculation of eigenstates. The method can be classified as a spectral expansion of a function of the Hamiltonian operator.

For approximating an analytic function $f(z)$ the spectral expansion possesses exponential convergence.¹⁰ Comparison of the Chebychev propagator to other propagation schemes has shown that the Chebychev expansion is usually superior in both accuracy and efficiency to other methods.²¹

These findings have led to a proliferation of the use of the algorithm and to the exploration of its range of validity. It was found that the original Chebychev algorithm can become unstable when the Hamiltonian operator \hat{H} is not Hermitian. A complex non-Hermitian Hamiltonian arises naturally when absorbing boundary conditions are introduced.^{22–28} The reason for the instability is that support for the Chebychev polynomials is on the real axis. Although the Chebychev method can tolerate some complex character²³ large complex eigenvalues of the Hamiltonian cause severe instability. Complex eigenvalues are also obtained for the Liouville operator in a dissipative environment.^{29,30} Solving the Liouville von Neumann equation for dissipative open systems was the motivation for developing an alternative propagation scheme which could tolerate complex eigenvalues.³¹

The new propagator was based on the Newtonian interpolation polynomial. The support points or interpolation points were located on a polygon in the complex plane therefore tolerating complex eigenvalues of the Liouville operator which are contained within the polygon. Using the theory of interpolation in the complex plane it can be shown that a uniform converging interpolation in a domain D is obtained when the interpolation points are located on the circumference of the domain.

The choice and ordering of the points is crucial to the stability of the algorithm. If two points are very close there is a division by a number close to zero in the divided difference algorithm Eq. (2.7). Evenly distributed points on the exterior of the polygon were obtained by a conformal mapping of the polygon onto a circle where evenly distributed points are easily obtained by symmetry considerations. An inverse transform distributed the points back onto the polygon. Ordering the points was found to be crucial to the stability of the algorithm, influencing directly the calculation of the divided difference coefficients. It was found that to obtain stability a complete staggering of points was required.³¹ The scheme was applied to the evolution operator in simulating photo-induced processes in solution^{32,33} and photo-induced desorption from metal surfaces.³⁴ Another application has been the calculating of the S matrix in reactive scattering using absorbing boundaries.^{35,36}

In practical applications the Newtonian based propagator was found to be hard to use. The difficulty could be traced to the Schwartz–Christoffel conformal mapping algorithm³⁷ which is required to obtain the uniformly distributed points on the circumference of the interpolation domain. The mapping algorithm severely limited the order of the Newtonian interpolation polynomial in the complex plane. This is in contrast to Newtonian interpolation on the real axis where no limit to the order of the polynomial was found.^{7,38} The present paper presents a new approach to defining the interpolation points termed Leja points,³⁹ which is able to overcome the difficulty in locating the interpolation points.

In parallel to these developments the original Chebychev expansion was generalized first by shifting the support from the real axis to a line shifted into the complex plane.¹⁶ This shift greatly enhances the stability of the method. The domain of stability becomes an ellipse in the complex plane.

Another alternative is to modify the recursion relation of the Chebychev polynomial by adding a damping term.⁴⁰ A more rigorous fix to the problem is to define a spectral expansion in the complex plane. The Faber polynomials which are a generalization of the Chebychev polynomials constitute such a set. With the use of the Faber polynomial it has recently been shown that a stable uniform approximation in the complex plane is possible.⁴¹

Before continuing a brief comparison of the two methods is appropriate. If for the Newtonian propagator the zeros of the Chebychev polynomial are chosen as sampling points the two methods are numerically equivalent.⁷ Formally, if the expansion coefficients in the Chebychev series are calculated by a Gaussian–Chebychev quadrature rule then the expansion becomes an interpolation formula mathematically equivalent to the Newtonian interpolation formula.⁷ For the practitioner it will be shown that the Newtonian method is more flexible when different functions of the Hamiltonian are required simultaneously.

The Newtonian method will be applied to calculate the mapping of a wave function by functions of the Hamiltonian operator \hat{H} , such as

$$\psi(t+t') = [e^{-i/\hbar \hat{H}t'}] \psi(t), \quad (2.3)$$

which is a mapping of a wave function from time t to time $t+t'$, and

$$R(E_L) = \left[\int_0^\infty e^{i/\hbar (E_L + E_i - \hat{H})t'} e^{-g(t)} dt \right] \psi_i, \quad (2.4)$$

which is the mapping of an initial ground surface vibrational state with energy E_i to a Raman function governed by the excited surface Hamiltonian, induced by the excitation frequency $\omega_L = E_L/\hbar$ and damping function $g(t)$.

To summarize, the basic idea underlying the algorithm is that approximating a function of the Hamiltonian is equivalent to approximating a scalar function in the domain of eigenvalues of \hat{H} .

A. Newtonian interpolation method

The propagation method is based on the Newtonian interpolation formula in which an analytic function $f(z)$ is approximated as a polynomial:

$$f(z) \approx \mathcal{P}_{N-1}(z) \equiv \sum_{n=0}^{N-1} a_n \prod_{j=0}^{n-1} (z - x_j). \quad (2.5)$$

By definition on the sampling points x_j , $f(x_j) \equiv \mathcal{P}(x_j)$. The coefficient a_n is the n th divided difference coefficient⁴² defined as

$$a_0 = f[x_0] = f(x_0),$$

$$a_1 = f[x_0, x_1] = \frac{f(x_1) - f(x_0)}{x_1 - x_0}, \quad (2.6)$$

$$a_k = f[x_0, x_1, \dots, x_k] = \frac{f(x_k) - \mathcal{P}_{k-1}(x_k)}{\prod_{j=0}^{k-1} (x_k - x_j)}. \quad (2.7)$$

To construct a propagator the interpolation formula is applied to the Hamiltonian operator:

$$\begin{aligned} f(\hat{H}) &\approx \mathcal{P}_{N-1}(\hat{H}) \\ &= a_0 \hat{\mathbf{I}} + a_1 (\hat{H} - x_0 \hat{\mathbf{I}}) + a_2 (\hat{H} - x_1 \hat{\mathbf{I}}) (\hat{H} - x_0 \hat{\mathbf{I}}) + \dots \\ &= \sum_{n=0}^{N-1} a_n \prod_{j=0}^{n-1} \hat{Q}_j = \sum_{n=0}^{N-1} a_n \prod_{j=0}^{n-1} (\hat{H} - x_j \hat{\mathbf{I}}). \end{aligned} \quad (2.8)$$

We still have the freedom to choose the function $f(z)$. The choice and order of the interpolation points, x_j is the crucial step in the algorithm.

B. Choosing interpolation points

The first step is to establish the domain D of eigenvalues of the Hamiltonian operator \hat{H} . Once the domain is defined the algorithm used to generate the interpolation points can begin.

(1) A line encircling the domain D in the complex plain is defined. For practical purposes it will be chosen as a polygon. The domain is scaled in size, without changing its shape, to make the interpolation process stable. While its exact size will be fixed in step 4, initial coordinates should be of the order of 1.

(2) Trial points $\{y_i\}$ are calculated to be equally distributed on the circumference contour of the domain D . The number of trial points is 1.5–3 times the number of requested interpolation points.

(3) The interpolation points $\{x_i\}_{i=0}^{N-1}$ are chosen from $\{y_i\}$. The first interpolation point can be chosen arbitrarily:

$$x_0 = y_0. \quad (2.9)$$

To avoid dividing by very small numbers, other interpolation points are chosen so they maximize the denominator of Eq. (2.7). After choosing n such points, the product

$$\mathcal{J}(y_i) = \prod_{j=0}^{n-1} |y_i - x_j| \quad (2.10)$$

is calculated for each trial point y_i . The trial point for which \mathcal{J} , Eq. (2.10), is maximal becomes x_n . If (2.10) goes to zero or infinity for large n 's, the size of D should be adjusted to correct that [e.g., scaled down if (2.10) overflows].

(4) The optimal interpolation points are calculated by normalizing the size of D . A point z in the center of the domain is chosen arbitrarily, and a normalizing factor is calculated by

$$\rho = \prod_{j=0}^{N-1} |z - x_j|^{1/N}. \quad (2.11)$$

Each of the x_j 's is then divided by ρ , to yield \tilde{z}_j . The result is N sampling points on the contour of a scaled domain \tilde{D} . The normalization is essential to keep (2.5) stable. If \tilde{D} is too small this will result in divergence of the divided differences (the a_k 's), while if it is too large it will diverge the product term in (2.5).

C. Propagation algorithm

After choosing the interpolation points, The Hamiltonian operator is shifted and scaled so all of its eigenvalues reside inside the domain \tilde{D} :

$$\tilde{\mathbf{H}} = (\hat{\mathbf{H}} - \bar{H}) \cdot \frac{1}{\sigma}. \quad (2.12)$$

\bar{H} is the center of the domain of eigenvalues of $\hat{\mathbf{H}}$, and σ is a scaling factor. To compensate for the change from $\hat{\mathbf{H}}$ to $\tilde{\mathbf{H}}$, the interpolation polynomial is used to approximate a scaled function $\tilde{f}(z) = f(z\sigma + \bar{H})$:

$$\begin{aligned} f(\hat{\mathbf{H}})\psi &\equiv \tilde{f}(\tilde{\mathbf{H}})\psi \\ &\approx \tilde{\mathcal{P}}_{N-1}(\tilde{\mathbf{H}})\psi \\ &\equiv a_0\psi + a_1(\tilde{\mathbf{H}} - \tilde{z}_0)\psi + a_2(\tilde{\mathbf{H}} - \tilde{z}_1)(\tilde{\mathbf{H}} - \tilde{z}_0)\psi \\ &\quad + a_3(\tilde{\mathbf{H}} - \tilde{z}_2)(\tilde{\mathbf{H}} - \tilde{z}_1)(\tilde{\mathbf{H}} - \tilde{z}_0)\psi + \dots \end{aligned} \quad (2.13)$$

with the \tilde{z}_k 's residing on the contour of \tilde{D} , and the a_k 's calculated by

$$a_0 = \tilde{f}(\tilde{z}_0), \quad (2.14)$$

$$a_k = \frac{\tilde{f}(\tilde{z}_k) - a_0 - \sum_{l=1}^{k-1} a_l (\tilde{z}_k - \tilde{z}_0) \cdots (\tilde{z}_k - \tilde{z}_{l-1})}{(\tilde{z}_k - \tilde{z}_0) \cdots (\tilde{z}_k - \tilde{z}_{k-1})}. \quad (2.15)$$

To calculate the product terms in (2.13) a recursive relation is used:

$$\begin{aligned} \phi_0 &= \psi, \\ \phi_1 &= (\tilde{\mathbf{H}} - \tilde{z}_0 \hat{\mathbf{I}})\phi_0, \\ \phi_{n+1} &= (\tilde{\mathbf{H}} - \tilde{z}_n \hat{\mathbf{I}})\phi_n. \end{aligned} \quad (2.16)$$

The final result is obtained by accumulating the sum:

$$\phi = \sum_{n=0}^{N-1} a_n \phi_n. \quad (2.17)$$

The sum is truncated when the residuum $a_N ||\phi_N||$ is smaller than a prespecified tolerance. Since the quality of the approximation of the function $f(\hat{\mathbf{H}})$ is equivalent to a scalar function in the domain D before performing the actual calculation the accuracy can be checked on the scalar function. Figure 1 shows contour maps of the accuracy of the interpolation for some test cases.

A few guidelines for choosing the interpolation points can be deduced from experience and from these figures.

(1) It becomes obvious that when using interpolation points residing only on the real axis (as in the original Chebyshev algorithm) the domain of stability is a small region around the real axis. Choosing the same number of points on the circumference of a rectangular domain leads to a much better coverage in the complex plain. If the domain contains all of the eigenvalues of the interpolated operator stability is assured for very long time steps. Figures 1(a) and 1(b) show the domain of convergence of the Chebyshev scheme.

(2) The number of trial points has to exceed the number of actual interpolation points. If too few trial points are used the interpolation becomes inaccurate, especially in the vicinity of the sharp corners of the domain. Higher order interpolation polynomials require more trial points, since the density of the points increases making the divided difference terms more sensitive to the choice of the interpolation points. The actual number of trial points needed for a low order ($N < 100$

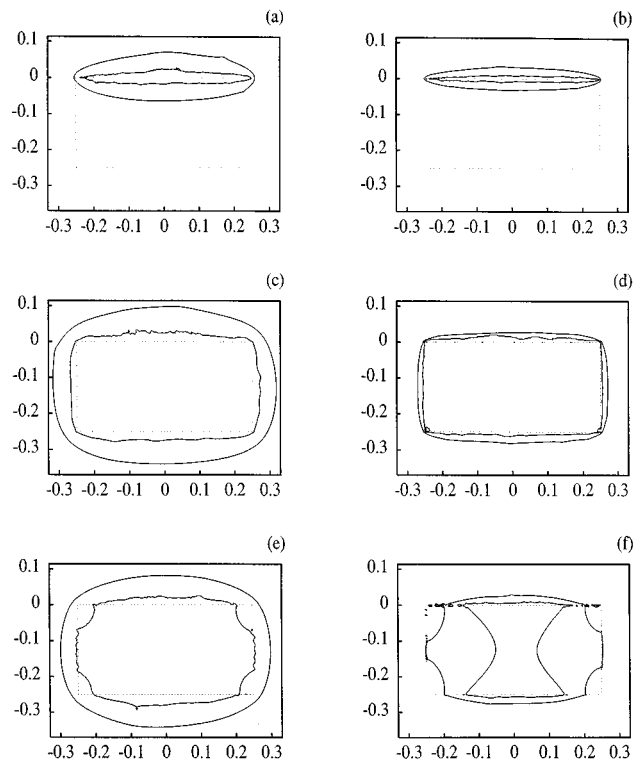


FIG. 1. Contour maps for the accuracy of the Newtonian interpolation. The approximated function is a propagator with a time step of 100 a.u. and a Hamiltonian with $\delta E = 0.5$ a.u. The inner line is the boundary of the domain in which the relative error of the interpolation is less than 10^{-5} ; the outer line is for relative error larger than 1 (stability boundary). (a) and (b) were calculated with the Chebyshev algorithm, with interpolation points on the real axis; (c)–(f) were calculated with Newtonian interpolation, with interpolation points on the dotted rectangle. The number of points used in each map is (a) 64, (b) 128, (c) 64 chosen from 96, (d) 200 chosen from 300, (e) 64 chosen from 67, and (f) 200 chosen from 210.

terms) polynomial is 1.5 times the number of trial points, while for higher order polynomials the ratio will be bigger (for an 800 term polynomial a ratio of 1:3 was needed). Too many trial points will slow the calculation, but this calculation is performed only once before the propagation cycle. Figures 1(c) compared to 1(e) and 1(d) compared to 1(f) show the effect of not choosing enough trial points on the convergence domain.

(3) Employing more interpolation points than is required for obtaining the desired accuracy inside the domain hampers the calculation. As a result the stability area shrinks and if some eigenvalues reside outside, but close to, the domain the accuracy is degraded. This is the reason why the Chebyshev algorithm is stable only for short time steps when an absorbing potential is employed, but diverges when using larger time steps which require higher order polynomials. For comparison, the results in Section III D were calculated using 2000 a.u. time steps (700 terms in the polynomial). The same calculations carried out with the Chebyshev algorithm diverged for time steps larger than 100 a.u. (64 terms). This effect can be seen by comparing Fig. 1(a) to 1(b) or 1(c) to 1(d).

III. PHOTODISSOCIATION DYNAMICS

The purpose of the calculation is to follow the photodissociation events of I_3^- from the initial thermal state on the ground surface to the final product $I_2^- + I$. The dynamics studied by the experiment is carried out in solution; therefore solvent degrees of freedom are also involved in the process. A full simulation requires the inclusion of many degrees of freedom. The approach followed in this study is to set a model of the encounter involving a limited number of degrees of freedom. Within this model a fully converged quantum mechanical calculation is carried out. Insight into the photodissociation process can be obtained by comparing the calculated observables with the experiment. Discrepancies between experiment and the model will point to the missing degrees of freedom in the calculation.

A. Simulation setup and initial wave functions

The model assumes I_3^- to be collinear and centrosymmetric. The bending motion is ignored; therefore only two degrees of freedom are considered. The rotation of the molecule is excluded from the calculations since a separation of time scales exists between the rotational and vibrational motion. This is true also for the bend modes. The influence of solvent degrees of freedom will be considered in a future study.⁴³

Three potential energy surfaces are required to simulate the photodissociation dynamics. The process is initiated on the ground electronic surface of I_3^- . A harmonic potential in the symmetric and antisymmetric stretch modes is used. The harmonic frequencies are adjusted to the measured values or to *ab initio* calculations.⁴⁴ Only small differences exist between these two sets of data. This description is appropriate for low excitation energies but considering the possibility of recombination events, where high excitation of the ground surface vibration is anticipated, the present description is not sufficient.

The excited potential energy surface was chosen to be in a LEPS form used previously.² The asymptotic I_2^- channels are fitted to a Morse potential form. This form fits well with spectroscopic measurements and *ab initio* calculations.

The excited surfaces are split due to spin-orbit interaction. The present calculations include only the transition to the upper excited surface. The vertical distance between the ground and the upper excited surface was adjusted to the absorption spectra. Attempts to calculate the vertical distance by *ab initio* methods were unsuccessful.

In order to simulate an experiment carried out at room temperature the simulation was assembled from a set of initial wave functions. These wave functions were calculated on the ground surface potential by the relaxation method.¹⁷ All vibrational levels up to an energy of 300 cm^{-1} were calculated. This means that at room temperature 61% of the population was accounted for in the simulation. It will be shown that this subset of the population is dominant in the experimental observations (see Tables I and II).

B. Pump pulse

The first step in the photodissociation event is induced by the pump pulse. Starting from a stationary state on the

TABLE I. The influence of the initial vibrational excitation on the population transferred to the excited surface. Excitation wavelength was 308 nm.

$A \setminus S$	0	1	2	3
0	18.6%	41.6%	27.3%	5.0%
1	17.1%	40.4%		
2	15.8%			

ground potential [Fig. 2(a)] amplitude is transferred to the excited surface potential by the coupling to the radiation field. The process is simulated by solving the coupled time dependent Schrödinger equation:

$$i\hbar \frac{\partial}{\partial t} \begin{pmatrix} \psi_e \\ \psi_g \end{pmatrix} = \begin{pmatrix} \hat{H}_e & -\epsilon \hat{\mu} \\ -\epsilon^* \hat{\mu} & \hat{H}_g \end{pmatrix} \begin{pmatrix} \psi_e \\ \psi_g \end{pmatrix}, \quad (3.1)$$

where initially all the amplitude is in the ground surface $\psi(0) = \psi_g$ in an initial vibrational eigenstate. $\hat{H}_{e/g}$ are the surface Hamiltonians. $\hat{\mu}$ is the electronic transition dipole and $\epsilon = \epsilon(t)$ is the time dependent field. Using a rotation frame $\epsilon(t) = \bar{\epsilon}(t)e^{-i\omega t}$ the excited state potential can be lowered by an amount equal to the laser's frequency ω resulting in a real crossing point with the ground potential surface. The resulting coupling between the shifted surfaces $\bar{\epsilon}(t)\hat{\mu}$ becomes a slowly varying Gaussian field of 60 fs FWHM. To account for time ordering in the propagator due to the non-stationary Hamiltonian during the pulse a first order Magnus approximation was used.⁴⁵

Under the experimental conditions the intensity is large enough that a significant fraction of the population is transferred to the excited surface. Considering individual initial vibrational states, the fraction transferred depends primarily on the symmetric stretch excitation. This effect is summarized in Table I.

The pump pulse used in the experiment was long in comparison to dynamics in the symmetric stretch mode on the excited surface. Significant coupling is present for a duration of ~ 180 fs [Figs. 2(b)–2(d)]. This means that photodissociation dynamics proceeds while amplitude is still fed to the excited surface. Most of this motion is along the symmetric stretch mode as opposed to dynamics leading toward bond cleavage, i.e., motion along the antisymmetric stretch, which is small.

The wave packet remaining on the ground electronic surface also becomes excited by the pulse creating a dynamical "hole."³³ Since the previous analysis of this effect included only the symmetric stretch degree of freedom we explicitly

TABLE II. The Boltzmann distribution of the initial vibrational states. Total population with up to 3 quanta in each mode is 82%.

$A \setminus S$	0	1	2	3
0	20.5%	12.0%	7.1%	4.1%
1	10.3%	6.0%	3.5%	2.1%
2	5.2%	3.0%	1.8%	1.0%
3	2.6%	1.5%	0.9%	0.5%

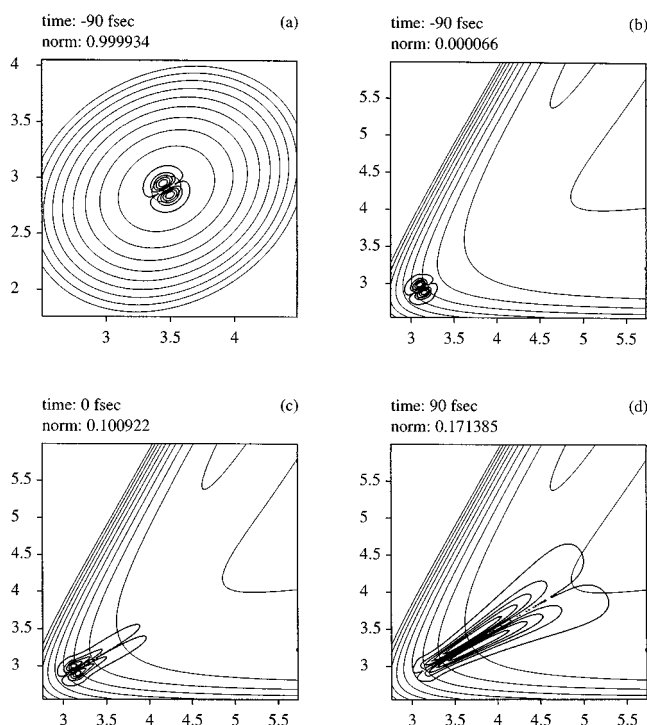


FIG. 2. Propagation of the wave packet during a 60 fs pump pulse. The initial state shown is the first excited state of the antisymmetric mode. (a) shows the wave function on the ground state at the very beginning of the pulse. (b) shows the excited surface wave function. (c) shows the wave function at the peak of the pulse and (d) is the wave function after most of the pulse is over. The scaling is in Ångstroms.

looked for possible excitation of the antisymmetric stretch mode in this two dimensional calculation. With the frequency, duration and intensity of the pulses used experimentally, no significant excitation of the antisymmetric stretch occurred on either potentials.

C. Raman spectrum

A complementary probe of the first stages of the dissociation dynamics is provided by the Raman spectra.⁴⁶ The Raman cross section is calculated from the half Fourier transform of the correlation function.^{47,46} This amounts to the overlap of the Raman wave function Eq. (2.4) with the final vibrational state:

$$\sigma_{if}(E_L) = \frac{8\pi E_S^3 E_L e^4}{9\hbar^6 c^4} |\langle R_i(E_L) | \hat{\mu} | \psi_f \rangle|^2, \quad (3.2)$$

where E_L is the excitation energy and E_S is the scattered energy. For each initial vibrational state ψ_i a Raman wave function $R_i(E_L)$ was calculated using the method of Section II, based on interpolating Eq. (2.4). The damping $g(t)$ function was taken from Ref. 48; its inclusion changed the observed spectrum very slightly. The Raman wave function shown in Fig. 3 is very similar to the wave packet created by the pump pulse [Fig. 2(c)]. Thus the Raman spectra and the resonative impulsive stimulated Raman scattering (RISRS) experiment carry complimentary information on the initial stage of the photodissociation.

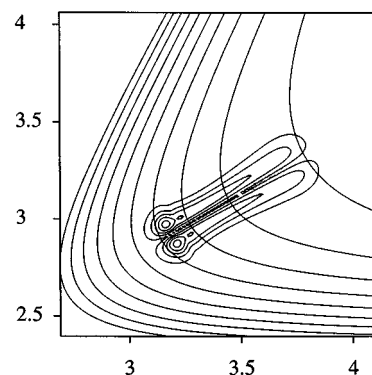


FIG. 3. The Raman wave function excited from $v=1$ in the antisymmetric stretch. The excitation energy E_L is on resonance with the transition. The propagation was stopped at a time of 3000 a.u. The scaling is in Ångstroms.

The Raman spectrum was composed from a Boltzmann average over the individual initial vibrations. Figure 4 shows a stick Raman spectrum at $T=300\text{K}$.

Examining the spectrum it can be seen that the antisymmetric stretch has a very small signature which increases for higher Raman shifts corresponding to longer propagation times on the excited surface. This is consistent with the shape of the Raman wave function which only spreads slightly in the antisymmetric direction. A similar picture is obtained in the real time propagation during the excitation in Sec. III B.

D. Dissociation dynamics

Once the pump pulse is over, the dynamics on the ground and excited surfaces decouple. Since the focus of the calculation is shifted to the products, free propagation of the wave function is carried out on the excited surface alone. The excited wave function $\psi_e(t_f)$ induced by the excitation pulse at time t_f described in Sec. III B was used as the initial state. The propagation was carried out by Eq. (2.3) with a time step of $t' = 2000$ a.u. Intermediate 50 fs snapshots of the evolving wave function were stored. Figures 5 and 6 show several snapshots starting from two different initial wave functions. (Also see Table III.)

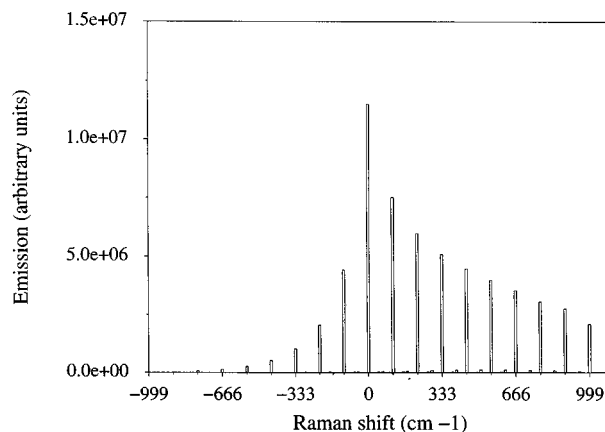


FIG. 4. The simulated Raman spectrum at $T=300\text{K}$ of I_3^- in solution.

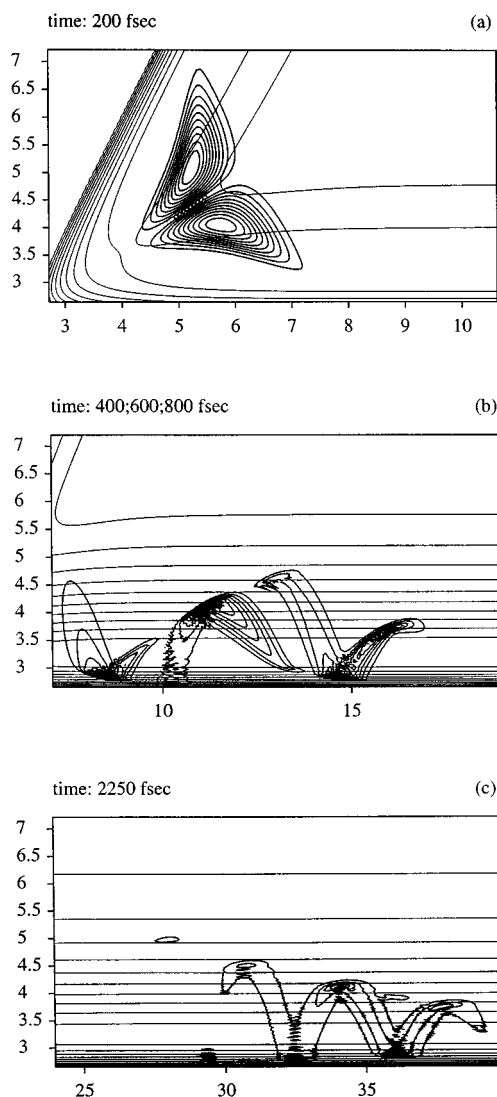


FIG. 5. Propagation of the wave packet $\psi_e(t)$ generated by the pump pulse, on the excited surface. The initial state $\psi_g(0)$ of the wave function is the first excited state of the antisymmetric mode. The scaling is in Ångströms.

At the early stage of the dynamics the motion is along the symmetric stretch direction, down the potential slope, across the saddle point and “uphill” in the direction of the three body dissociation. Only when the wave function crosses the saddle point does motion in the direction of the antisymmetric stretch becomes significant. This is the stage of the dynamics, leading eventually to bond cleavage.

The wave function that was initiated as an antisymmetric eigenstate on the ground surface is “better suited” for such motion, and enters the second stage earlier, falling rapidly into the exit channels without ascending much into three body dissociation [Fig. 5(a)]. On the other hand, the wave function that is initially centrosymmetric continues ascending much further before bifurcating into the exit channels [Fig. 6(a)].

The wave function enters the exit channels with a substantial amount of excess energy (~ 1.2 eV), which translates into two asymptotic modes: vibration of the I_2^- fragment, and translation of the I atom away from the I_2^- molecule. Coher-

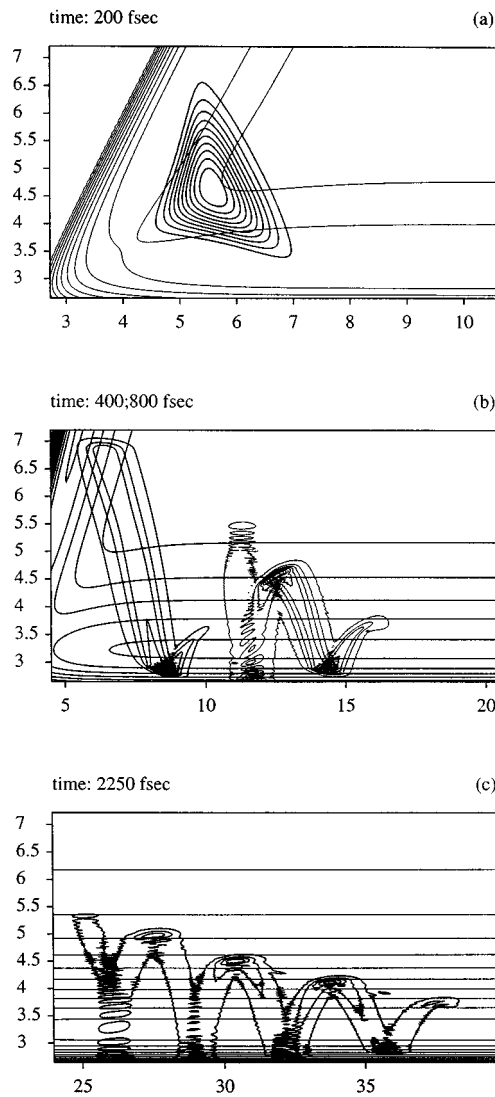


FIG. 6. Propagation of the wave packet $\psi_e(t)$ generated by the pump pulse, on the excited surface. The initial state $\psi_g(0)$ of the wave function is the first excited state of the symmetric mode. The first wave function in (b) is “chopped” at the top of the frame by an absorbing potential. The scaling is in Ångströms.

ent vibrational motion of the antisymmetric wave function is seen clearly in Fig. 5(b), and less evidently in 6(b).

After longer propagation, the wave function is no longer compact because of the large distribution in translational energy which smears the wave packet into a long “snake” [Figs. 5(c) and 6(c)]. Due to the limited bandwidth of the exciting pulse a strong correlation exists between the vibration and translation modes of the excited wave function. Accordingly the most rapidly propagating portions of the reactive packet are least excited vibrationally and vice versa, while the slower parts have greater vibrational energy.

Analysis of the energy distribution of the wave function after it reached the asymptotic region of the potential is shown in Fig. 7. The broader distribution for the symmetric wave function comes from the higher ascent of this wave function in the three body dissociation direction, which results in higher vibrational energy in the exit channel.

TABLE III. Typical parameters of propagation in a.u.

Ground potential surface for I_3^- ^a			
$V_g(r_{ab}, r_{bc}) = \frac{1}{2}k(r_{ab}-r^{eq})^2 + \frac{1}{2}k(r_{bc}-r^{eq})^2 + \chi(r_{ab}-r^{eq})(r_{bc}-r^{eq})$			
$k = 0.04598$	$\chi = 0.01323$	$r^{eq} = 5.480$	
Excited potential surface for I_3^- ^a			
$V_e(r_{ab}, r_{bc}, r_{ac}) = \Delta E_0 + Q_1 + Q_2 + Q_3 - (J_1^2 + J_2^2 + J_3^2 - J_1 J_2 - J_2 J_3 - J_3 J_1)^{1/2}$			
$Q_i = \frac{1}{2}[{}^1E(r_i) + {}^3E(r_i)]$	${}^1E(r_i) = {}^1D[1 - e^{-\beta(r_i - r^{eq})}]^2 - {}^1D$		
$J_i = \frac{1}{2}[{}^1E(r_i) - {}^3E(r_i)]$	${}^3E(r_i) = {}^3D[1 + e^{-\beta(r_i - r^{eq})}]^2 - {}^3D$		
${}^1r^{eq} = 6.104$	${}^1\beta = 0.6138$	${}^1D = 0.0404$	
${}^3r^{eq} = 5.637$	${}^3\beta = 0.5292$	${}^3D = 0.0371$	$\Delta E_0 = 0.1361$
Excited potential for I_2^- ^b			
$V_e(r) = D[1 - e^{-\beta(r - r^{eq})}]^2 - D + \Delta E_0$			
$r^{eq} = 9.128$	$\beta = 0.7091$	$D = 3.675 \times 10^{-4}$	$\Delta E_0 = 0.1361$
Absorbing potential ^c			
$V(\bar{y}) = -i \cdot A \cdot N \cdot e^{-2/\bar{y}}$	$\bar{y} = (y - y_i)/(y_f - y_i)$		
$A = 0.018$	$N = 13.22$	$y_i = 8.94$	$y_f = 9.69$
Electromagnetic field			
$\epsilon(t) = \bar{\epsilon}(t)e^{i\omega t}$		$\bar{\epsilon}(t) = A e^{(-2 \ln 2 / \tau^2)(t - t_0)^2}$	
$\omega = 0.1479$	$A = 2.5 \times 10^{-4}$	$\tau = 2400$	$t_0 = 4800$
Dipole function	$\hat{\mu} = a$	$a = 3.7$	
Mass weighted grid			
$x = a \cdot r_{ab} + b \cdot \cos \beta \cdot r_{bc}$		$y = b \cdot \sin \beta \cdot r_{bc}$	
$a = \sqrt{\frac{2}{3}}$	$b = \sqrt{\frac{2}{3}}$	$\beta = \frac{\pi}{3}$	
$\Delta x = 1.2 \times 10^{-2}$	$N_x = 1024$	$x_{\min} = 6.24$	
$\Delta y = 1.2 \times 10^{-2}$	$N_y = 512$	$y_{\min} = 3.42$	
Mass	$M = 127$ a.m.u.		
Propagation			
With pulse	$\Delta t = 100$	$N_t = 100$	Order = 55
Without pulse	$\Delta t = 2000$	$N_t = 10$	Order = 700
Tolerance	10^{-6}		

^aSee Ref. 4.^bSee Ref. 50.^cSee Ref. 26.

E. Probe pulse

The probe pulse in the photodissociation experiment of I_3^- is tuned to the absorption of the product I_2^- in the range of 600–800 nm. It is important to state at the outset that with significant vibrational excitation the nascent product absorption spectrum should be significantly broadened. This transition is to a dissociative state of I_2^- . This means that the probe is only sensitive to the vibrational motion of the product. To obtain the absorption signal of the probe pulse the impulsive limit can be employed in weak fields³³ leading to

$$\begin{aligned} \Delta E &= -\hbar \omega \Delta N_g \\ &= -\hbar \omega \int_R \int_r \mathcal{W}(\mathbf{r}, \tau_{\text{pr}}) |\psi_e(\mathbf{r}, R, t_{\text{pr}})|^2 d\mathbf{r} dR, \end{aligned} \quad (3.3)$$

where t_{pr} is the probing time, and the window function \mathcal{W} becomes

$$\mathcal{W}(\mathbf{r}, \tau_{\text{pr}}) = (\hbar W \tau_{\text{pr}})^2 \left(\frac{\sin(\Delta(\mathbf{r}) \tau_{\text{pr}} / \hbar)}{\Delta(\mathbf{r}) \tau_{\text{pr}} / \hbar} \right)^2, \quad (3.4)$$

where τ_{pr} is the width of the probe pulse, $2\Delta(\mathbf{r}) = \mathbf{V}_e(\mathbf{r}) - \mathbf{V}_g(\mathbf{r}) - \hbar \omega_{\text{pr}}$ is the difference between the excited and ground surface potentials of I_2^- , and W is the integrated intensity of the pulse.

Examining Eq. (3.3) it is immediately apparent that the probe pulse is sensitive only the vibrational position density at the point of resonance of the probe pulse ω_{pr} . Once the evolving wave packet reaches the asymptotic channel it can be decomposed into vibrational and translational eigenstates:

$$\psi_e(r, R, t) = \sum_{n,i} c_{ni}(t) \phi_n(r) \chi_i(R). \quad (3.5)$$

These eigenstates can be propagated by phase shifting, allowing propagation of the asymptotic wave function to very long times with almost no computational cost. The accuracy

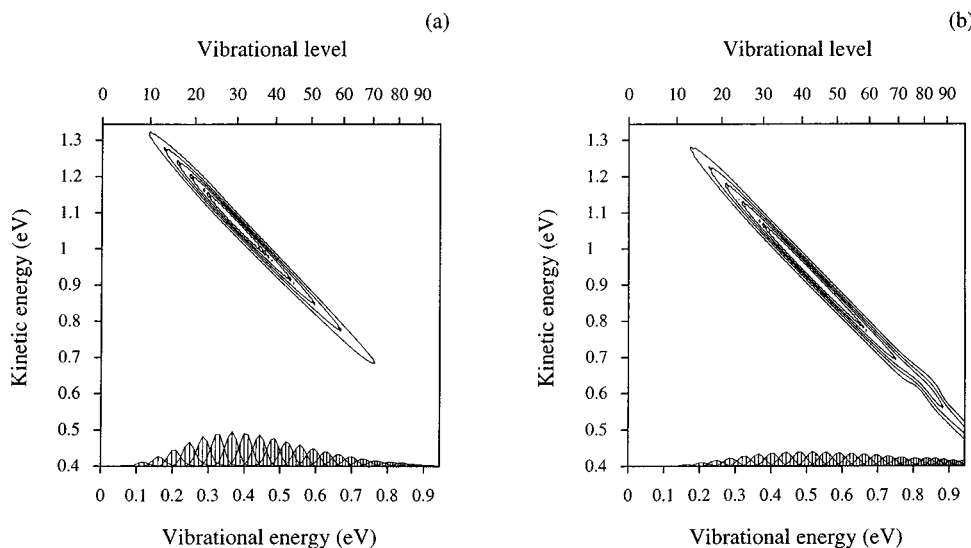


FIG. 7. The product energy distribution of the photodissociation product. The probability density as a function of the vibrational–translational state is shown. The contours depict a projection of the function on the vibrational–translational plane, and the bottom graphs show a projection on the vibrational–probability plane. In (a) the initial state of the wave function is the first excited state of the antisymmetric mode. In (b) the initial state of the wave function is the first excited state of the symmetric mode.

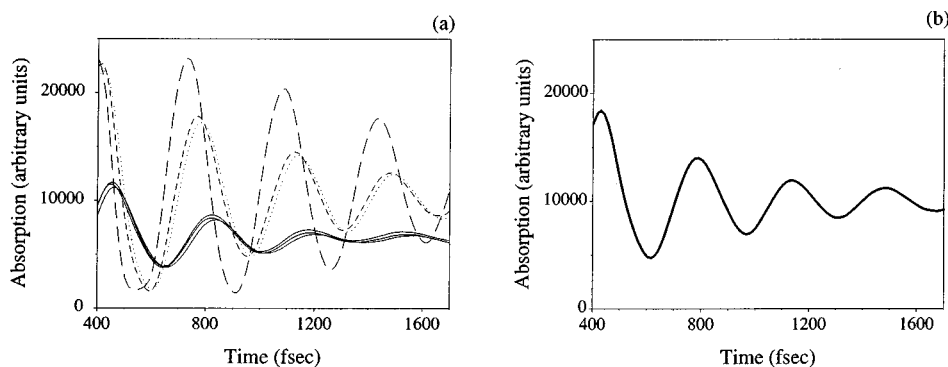


FIG. 8. The transient absorption of the I_2^- products with a probe pulse of 60 fs and a wavelength of 620 nm: (a) a comparison of the signal originating from different initial wave packets. All signals are normalized with respect to the excited state population. The solid lines represent the pure symmetric stretch excitations $v=0,1,2$ which all bunch together. The antisymmetric stretch excitations are represented as broken lines: $v=1$ in the antisymmetric stretch (dotted), $v=1$ in the antisymmetric stretch and $v=1$ in the symmetric stretch (dashed line), $v=2$ in the antisymmetric stretch and $v=0$ in the symmetric stretch (long dashed line). (b) Simulated transient absorption spectra at a temperature of $t=300$ K obtained by a Boltzmann average on six initial vibrational states (61% of the population).

of this procedure was checked by comparison to a direct propagation and was found satisfactory (90% overlap for a duration of 500 fs). Integrating over the translational degrees of freedom a reduced vibrational density operator is obtained, $\rho(v,v')$. It was found that the simulated probe signal was solely determined by the reduced vibrational density once the wave function reached its asymptotic channel.

Examining Fig. 8 it is clear that the larger modulations of the probe signal are induced upon excitation of the antisymmetric stretch mode. This must be associated with the compact nature of the reactive packet generated from these initial states. The phase of the signal is also shifted to earlier times because the wave packet enters the exit channel earlier.

In general the signal decays in time due to the significant anharmonic motion of the I_2^- vibration which is created in a highly excited state. The modulations from the averaged thermal signal are somewhat smaller since the individual contributions are slightly out of phase.

IV. DISCUSSION

The calculation methods developed in this study are constructed in order to gain insight into the photodissociation dynamics. The computation is designed to address more than one experimental probe, in particular the relations between frequency resolved probes and time dependent probes. The simulation incorporated realistic pulse durations for the pump and probe interactions. The drawback of the current calculation is that the influence of the surrounding solvent is absent. Within a quantum mechanical framework the influence of the solvent could be incorporated by a reduced description. This means solving the Liouville von Neumann equation.³³ The propagation methods developed in Sec. II are suited for the dissipative Liouville propagation, which also possesses complex eigenvalues. Work in this direction is in progress.

Another alternative is to employ classical MD methods,⁴ or a mixture of quantum and classical methods. The drawback of the classical MD approach is that quantum interferences which determine the energy of the excited surface

wave packet induced by a long pulse are absent. The advantage of MD is the facile implementation of solvent effects including molecular details of the solvent.

It is important to reiterate that inclusion of vibrationally excited states of the reactant into the model has proven to be of utmost importance. The effects of vibrational excitation on the reactants are important to incorporate into our modeling and interpretation of the experiments. The extremely large effect that the excitation in the asymmetric stretching motion has on every aspect of the photochemical outcome, be it vibrational excitation in the products, the emergence time of isolated fragments, or the depth of modulation in the transient spectrum, underscores this clearly.

In the earlier report² which considered instantaneous excitation from the vibrational ground state, an effort was made to predict the effects of solvation on the dynamics. The emerging wave packet was qualitatively divided into “early exiting portions” and “late exiting portions.” Furthermore the hypothesis was presented that these somewhat ill-separated portions of the density would fare very differently with the solvent shell which surrounds the molecule. The former which enters at an early stage into the exit channel, i.e., rapidly decides which two nuclei will become I_2^- , should see moderate interference of the solvent in the vibrational dynamics of the fragment. The latter, in contrast, could be completely dephased by a head-on collision with solvent along the symmetric stretch, and lead to negligible contributions to any vibrational coherence in the products.

Including the various vibrational states in the model amplifies this concept, and introduces an inhomogeneous aspect into the dynamics, where at the outset we have well defined subpopulations that are predicted to exhibit very different reaction dynamics, including the effect of the solvent shell. Thus, the excited vibrational levels along the asymmetric stretch become the designated early exiting populations, and the vibrationless asymmetric stretch population clearly the late exciting portion of the population. It is found that after the amplitude separated into the exit channels a reduced vibrational density is sufficient to describe the dynamics. This

further allows us to predict that the contributions to the coherent vibrations and spectral modulations in triiodide dissociation in liquids could be dominated by population initially excited along the asymmetric stretch, which should in turn be enhanced by increasing the temperature.

It is interesting to point out the distinct roles played by vibrational excitation into the symmetric and asymmetric stretches in molding both the dynamics and absorption spectroscopy of I_3^- . In light of dynamical interpretation of spectroscopy it is customary to assume that vibrational excitation which leads to strong changes in the absorption spectrum will have a large effect on the ensuing dynamics. Here we are faced with the somewhat counterintuitive situation where excitation in the dark mode is exclusively influential in the dynamics.

But beyond considering the effect of vibrational excitation alone, it is important to point out that while the source of influence is the vibrational motion, the real driving force for the diverging chemical dynamical paths here is the breaking of molecular symmetry,⁴⁹ prior to photoexcitation. While in isolation the triiodide ion is predicted to be linear and centrosymmetric, previous reports in the literature deal with cases where solvation may lead to a breaking of symmetry. In many crystal lattices the triiodide ion is either bent or asymmetrically displaced leading to substantial changes in the electronic spectrum. More recently Myers and co-workers⁴⁸ have studied the resonance Raman spectra of I_3^- in several organic solvents, and have concluded that the appearance of weak overtones of the asymmetric stretch in the spectra of some of these solvents indicates that centrosymmetry may already be broken due to interactions with the solvent or the counterions. In view of the results presented here, it is hard to overemphasize the crucial effect such a symmetry breaking might have on the dynamics of triiodide dissociation in solution.

This study demonstrates the importance of quantum dynamical calculations in gaining insight on a complicated chemical encounter even in solution. The main asset of the computational methods developed in this study are their flexibility to address different types of experimental probes. These can be time dependent such as the spectral modulations of the product, or time independent such as the absorption or Raman spectrum. The method can be extended beyond the perturbative limit of the light matter interaction. Through the calculation of the expectation value of the dipole operator frequency and time resolved experiments can be simulated.

ACKNOWLEDGMENTS

This research was supported by the Israel Science Foundation administered by the Israel Academy of Science. The Fritz Haber Research Center is supported by the Minerva Gesellschaft für die Forschung, GmbH München, FRG.

- ¹ U. Banin, A. Waldheim, and S. Ruhman, *J. Chem. Phys.* **96**, 2416 (1992).
- ² U. Banin, R. Kosloff, and S. Ruhman, *Isr. J. Chem.* **33**, 141 (1993).
- ³ U. Banin and S. Ruhman, *J. Chem. Phys.* **98**, 4391 (1993).
- ⁴ I. Benjamin, U. Banin, and S. Ruhman, *J. Chem. Phys.* **98**, 8337 (1993).
- ⁵ A. Bartana, U. Banin, S. Ruhman, and R. Kosloff, *Chem. Phys. Lett.* **229**, 211 (1994).
- ⁶ N. Pugliano, D. K. Palit, A. Z. Szarka, and R. M. Hochstrasser, *J. Chem. Phys.* **99**, 7273 (1993).
- ⁷ R. Kosloff, *Annu. Rev. Phys. Chem.* **45**, 145 (1994).
- ⁸ D. Kosloff and R. Kosloff, *J. Comp. Phys.* **52**, 35 (1983).
- ⁹ R. Kosloff, in *Numerical Grid Methods and Their Application to Schrödinger's Equation*, edited by C. Cerjan (Kluwer, The Netherlands, 1993), p. 175.
- ¹⁰ H. Tal-Ezer and R. Kosloff, *J. Chem. Phys.* **81**, 3967 (1984).
- ¹¹ R. Kosloff, *J. Phys. Chem.* **92**, 2087 (1988).
- ¹² D. J. Kouri, M. Arnold, and D. J. Hoffman, *Chem. Phys. Lett.* **203**, 96 (1993).
- ¹³ W. Zhu, Y. Huang, D. J. Kouri, C. Chandler, and D. J. Hoffman, *Chem. Phys. Lett.* **217**, 73 (1994).
- ¹⁴ B. Hartke, R. Kosloff, and S. Ruhman, *Chem. Phys. Lett.* **158**, 238 (1989).
- ¹⁵ Y. Huang, W. Zhu, D. J. Kouri, and D. J. Hoffman, *Chem. Phys. Lett.* **214**, 451 (1993).
- ¹⁶ D. J. Kouri, W. Zhu, Y. Hoang, and D. J. Hoffman, *Chem. Phys. Lett.* **220**, 312 (1994).
- ¹⁷ R. Kosloff and H. Tal-Ezer, *Chem. Phys. Lett.* **127**, 223 (1986).
- ¹⁸ D. Neuhauser, *J. Chem. Phys.* **93**, 2611 (1990).
- ¹⁹ D. Neuhauser, *J. Chem. Phys.* **100**, 5076 (1994).
- ²⁰ M. R. Wall and D. Neuhauser, *J. Chem. Phys.* **102**, 8011 (1995).
- ²¹ C. Leforestier, R. Bisseling, C. Cerjan, M. Feit, R. Friesner, A. Guldberg, A. D. Hammerich, G. Julicard, W. Karrlein, H. Dieter Meyer, N. Lipkin, O. Roncero, and R. Kosloff, *J. Comp. Phys.* **94**, 59 (1991).
- ²² C. Leforestier and R. E. Wyatt, *Chem. Phys. Lett.* **78**, 2334 (1983).
- ²³ R. Kosloff and D. Kosloff, *J. Comp. Phys.* **63**, 363 (1986).
- ²⁴ D. Neuhauser and M. Baer, *J. Chem. Phys.* **90**, 4351 (1989).
- ²⁵ M. S. Child, *Mol. Phys.* **72**, 89 (1991).
- ²⁶ A. Vibok and G. G. Balint-Kurti, *J. Phys. Chem.* **96**, 7615 (1992).
- ²⁷ G. G. Balint-Kurti and A. Vibok, in *Numerical Grid Methods and Their Application to Schrödinger's Equation*, edited by C. Cerjan (Kluwer, The Netherlands, 1993), p. 412.
- ²⁸ C. W. MacCurdy and C. K. Stround, *Comp. Phys. Commun.* **63**, 323 (1991).
- ²⁹ G. Lindblad, *Commun. Math. Phys.* **48**, 119 (1976).
- ³⁰ R. Alicki and K. Landi, *Quantum Dynamical Semigroups and Applications* (Springer, Berlin, 1987).
- ³¹ M. Berman, R. Kosloff, and H. Tal-Ezer, *J. Phys. A* **25**, 1283 (1992).
- ³² A. Bartana, R. Kosloff, and D. Tannor, *J. Chem. Phys.* **99**, 196 (1993).
- ³³ U. Banin, A. Bartana, S. Ruhman, and R. Kosloff, *J. Chem. Phys.* **101**, 8461 (1994).
- ³⁴ P. Saalfrank, R. Baer, and R. Kosloff, *Chem. Phys. Lett.* **230**, 463 (1994).
- ³⁵ S. Aurbach and C. Leforestier, *Comp. Phys. Comm.* **78**, 55 (1994).
- ³⁶ S. M. Auerbach and W. H. Miller, *J. Chem. Phys.* **100**, 1103 (1994).
- ³⁷ L. M. Trefethen, *J. Sci. Stat. Comput.* **1**, 82 (1980).
- ³⁸ U. Peskin, R. Kosloff, and N. Moiseyev, *J. Chem. Phys.* **100**, 8849 (1994).
- ³⁹ Lotharreichel, *Bite* **30**, 332 (1990).
- ⁴⁰ V. A. Mandelshtam and H. S. Taylor, *J. Chem. Phys.* **103**, 2903 (1995).
- ⁴¹ Y. Hoang, D. J. Kouri, and D. J. Hoffman, *J. Chem. Phys.* **101**, 10493 (1994).
- ⁴² M. Abramowitz and I. A. Stegun, *Handbook of Mathematical Functions* (Dover, New York, 1972).
- ⁴³ R. Kosloff, G. Ashkenazi, and S. Ruhman, *Femtochemistry*, The Lussane Conference, edited by M. Chergui (unpublished).
- ⁴⁴ D. Danovich, J. Hrusak, and S. Shaik, *Chem. Phys. Lett.* **233**, 249 (1995).
- ⁴⁵ H. Tal Ezer, R. Kosloff, and C. Cerjan, *J. Comp. Phys.* **100**, 179 (1992).
- ⁴⁶ S. O. Williams and D. G. Imre, *J. Phys. Chem.* **92**, 3363 (1988).
- ⁴⁷ D. J. Tannor and E. J. Heller, *J. Chem. Phys.* **77**, 202 (1982).
- ⁴⁸ A. E. Johnson and A. B. Myers, *J. Chem. Phys.* **102**, 3519 (1995).
- ⁴⁹ R. Bianco and J. T. Hynes, *J. Chem. Phys.* **102**, 7885 (1995).
- ⁵⁰ E. C. M. Chen and W. E. Wentworth, *J. Phys. Chem.* **89**, 4099 (1985).